npj | digital medicine

Article

Published in partnership with Seoul National University Bundang Hospital

https://doi.org/10.1038/s41746-025-01466-9

Wearable microfluidic biosensors with haptic feedback for continuous monitoring of hydration biomarkers in workers

Check for updates

Julia C. Spinelli[1,11], Brandon J. Suleski[1,11], Donald E. Wright[1,11], Joseph L. Grow[1], Gabriel R. Fagans[1], Maura J. Buckley[1], Da Som Yang[2], Kaitao Yang[1], Steven M. Beil[1], Jessica C. Wallace[1], Thomas S. DiZoglio[1], Jeffrey B. Model[1,2], Shirley Love[1], David E. Macintosh[1], Alan P. Scarth[1], Matthew T. Marrapode[1], Corinna Serviente[3,4], Raudel Avila[5], Barrak K. Alahmad[6], Michael A. Busa[3,4], John A. Wright Jr[1,2], Weihua Li[1,2], Douglas J. Casa[7], John A. Rogers[2,8,9,10] ✉, Stephen P. Lee[1,2] ✉, Roozbeh Ghaffari[1,2,8] ✉ & Alexander J. Aranyosi[1,2] ✉

Real-time monitoring of hydration biomarkers in tandem with biophysical markers can offer valuable physiological insights about heat stress and related thermoregulatory response. These metrics have been challenging to achieve with wearable sensors. Here we present a closed-loop electrochemical/biophysical wearable sensing device and algorithms that directly measure whole-body sweat loss, sweating rate, sodium concentration, and sodium loss with electrode arrays embedded in a microfluidic channel. The device contains two temperature sensors for skin temperature and thermal flux recordings, and an accelerometer for real-time monitoring of activity level. An onboard haptic module enables vibratory feedback cues to the wearer once critical sweat loss thresholds are reached. Data is stored onboard in memory and autonomously transmitted via Bluetooth to a smartphone and cloud portal. Field studies conducted in physically demanding activities demonstrate the key capabilities of this platform to inform hydration interventions in highly challenging real-world settings.

Extreme heat due to climate change poses a significant threat to physiological thermoregulation and could trigger a variety of acute and chronic health conditions, particularly for workers who lack protection from the heat[1]. In addition to the short-term risks of heat exhaustion and heat stroke, recent studies have linked heat exposure to several morbidities[1–4] including cardiovascular, respiratory, and kidney diseases[1,5–7]. The onset of chronic kidney disease caused by dehydration due to heat stress episodes is rapidly growing, particularly in physically demanding occupations, sports, and daily activities[8,9]. The threats of heat exposure and dehydration are particularly high in low-to-middle-income countries in tropical environments with high physical workloads and limited safety regulations[10]. In physically demanding work, there may be exposure to radiating heat sources in indoor environments, limited ventilation within personal protective equipment (PPE), and lack of awareness to rehydrate, which further compounds health risks associated with extreme heat[11,12]. Heat has also been shown to negatively influence decision making as well as psychomotor and perceptual task performance[13]. A meta-analysis reports a 1% increase in injuries per 1 increase in temperature and a 17.4% increase during heat waves[14]. OSHA

[1]Epicore Biosystems, Inc, Cambridge, MA, USA. [2]Querrey-Simpson Institute for Bioelectronics, Northwestern University, Evanston, IL, USA. [3]Institute for Applied Life Sciences, University of Massachusetts Amherst, Amherst, MA, USA. [4]Department of Kinesiology, University of Massachusetts Amherst, Amherst, MA, USA. [5]Department of Mechanical Engineering, Rice University, Houston, TX, USA. [6]Department of Environmental Health, Harvard T.H. Chan School of Public Health, Harvard University, Boston, MA, USA. [7]Department of Kinesiology, University of Connecticut, Storrs, CT, USA. [8]Department of Biomedical Engineering, Northwestern University, Evanston, IL, USA. [9]Department of Mechanical Engineering, Northwestern University, Evanston, IL, USA. [10]Departments of Neurological Surgery, Chemistry, Electrical Engineering and Computer Science, Northwestern University, Evanston, IL, USA. [11]These authors contributed equally: Julia C. Spinelli, Brandon J. Suleski, Donald E. Wright. ✉e-mail: jrogers@northwestern.edu; stever@epicorebiosystems.com; rooz@northwestern.edu; aja@epicorebiosystems.com

recognizes that heat-related injuries and fatalities are likely underreported[15]. It is commonly understood that heat illness symptoms including tiredness, nausea, headache, and muscle cramps may be mistaken to be another form of injury or illness and/or occur when the worker is not at work and that workplace accidents may actually be the downstream result of undetected heat stress and dehydration[14]. Proper hydration is the single most important and economically feasible mitigation strategy against occupational heat strain[16]. However, people routinely underestimate their own fluid loss due to sweat production[17], and the perception of thirst is negligible below 1–2% body mass loss[18], at which point significant physical and cognitive deficits may already be present[19–21]. Novel sensor technologies that continuously monitor and report sweat loss along with personalized biometric data and micro-environmental exposures will be invaluable for actionable rehydration strategies to become standard practice.

Conventional strategies for heat stress management have relied on monitoring local Wet Bulb Globe Temperature (WBGT) devices or tracking weather patterns and heat index[22]. WBGT takes into account temperature, humidity, wind speed, and solar radiation. However, these monitors must be placed in close proximity of workers and require expertise to interpret data[23]. An alternative approach uses the National Weather Service's (NWS) Heat Index Chart, which assigns a risk level based on a combination of humidity and temperature and provides general guidelines for water consumption and work-rest schedules. Although effective in helping raise awareness, these population-based guidelines have limited utility for real-time individualized interventions and typically underestimate the impact of heat exposure. Moreover, blanket interventions do not account for individualized differences in physiological response nor the metabolic demands of each occupation on thermoregulation and sweat loss[12,23]. Another widely used tool for monitoring hydration status is based on the analysis of urine samples[24,25]. While urine-specific gravity represents a personalized analytical approach, access to urine is cumbersome and only offers a snapshot in time of hydration status, limiting the utility of this method for continued use throughout the workday. Moreover, none of these approaches provides quantitative insight into fluid intake needs.

Recent advances in electrochemical sensors and miniaturized bioelectronics have enabled real-time and non-invasive measurement of sweat dynamics and biomarkers associated with hydration status[26–33], disease progression[34], metabolic and hormonal status[35–37], and stress[38,39]. These sweat-sensing systems have established multimodal biochemical monitoring coupled with biophysical metrics[40] to support performance and physiology studies within controlled settings. Multiple sweat biomarkers, such as sweat sodium, estradiol, cortisol, and ethanol, are now quantifiable in sweat and correlated to blood serum levels, as a result of decade-long research and translational efforts underway[33]. Although innovation in this field has been rapid, existing solutions do not meet the needs of workers. In particular, existing sweat sensing devices do not provide autonomous and passive feedback to the wearer in response to excessive sweat loss measurements, in real-time. Existing wearable devices have not integrated contextual data streams, such as skin temperature, thermal flux, and motion measurements in conjunction with sweat biomarkers. Moreover, many sweat sensing devices are not suitable for real-world ambulatory deployments in extreme, uncontrolled environments consisting of high temperatures (40–65 °C) and extreme humidity (80–100%), where rigorous body movements and long durations of wear on the skin (1–12 h) are critical requirements. Only a few validation studies have deployed wearable sweat sensors in uncontrolled environments and even fewer wearable devices have been tested for accuracy (versus ground truth measurements) in large scale field studies[31,41,42]. Finally, existing solutions do not provide group data at the organizational level to empower health and safety professionals to act on an organization's overall hydration needs.

In this Article, we report a multimodal wearable electrochemical/biophysical sensing (EBS) device that continuously monitors whole-body sweat loss, sodium concentration, and sodium loss, in tandem with skin temperature, thermal flux, and movement signatures. The EBS device measures sweat biomarkers by capturing microliter quantities of sweat directly from the skin and utilizes an array of ultrathin interdigitated electrodes within a microchannel to compute the electrical impedance of excreted sweat and the extent of its propagation into the microfluidic channels. An onboard microprocessor and algorithms compute the quantity of sweat loss and sodium concentration. This information is stored in memory along with dual temperature readings (on the skin-facing and externally facing sides of the device) and motion data. To achieve autonomous feedback to the wearer, the EBS device exploits an onboard haptics motor that is triggered to vibrate briefly for each 500 mL of sweat lost and continuously once the wearer experiences excessive sweat loss (2% sweat loss per body weight), thereby informing the wearer about real-time sweat loss, which is associated with risk of dehydration and cognitive deficit[19–21]. Furthermore, the EBS device's hardware and mobile software user interfaces were designed to proactively improve hydration practices. Benchtop testing and on-body field studies of subjects wearing PPE during intense physical exercise highlight the unique capabilities of this platform.

Results

Electrochemical/biophysical sensing design and architecture

The EBS device consists of a disposable microfluidic substrate that collects perfused sweat from skin coupled to a reusable electronic module that measures sweat volume, sweat conductance, skin temperature, thermal flux, and motion, and provides real-time haptic feedback to the wearer in response to specific sweat loss thresholds (Fig. 1a). The microfluidic substrate consists of multiple layers of materials, including a patterned skin adhesive that allows sweat collection from a defined skin surface area (~115 mm^2), an electrode array comprised of ultrathin, flexible Ag/AgCl (21 μm thick) tuned for measuring sweat salinity and volume of collected sweat, a multi-layer microfluidic channel made of thermoplastic polyurethane aligned with the electrode array that fills as the wearer produces and excretes sweat, an overlaid cotton and adhesive skirt material for comfort and improved adhesion, a nylon clip for the electronic module, and intermediate adhesive layers to hold everything together. The fluidic channel is 240 μm tall and 1.5 mm wide, and the fluidic substrate overall is 1.14 mm thick (not including the clip, which is the height of the electronic module at its thickest point). The Ag/AgCl electrodes were printed in an interdigitated geometry to interface with the microchannel flow path and the sweat flowing inside. The dynamic flow of sweat through this microchannel makes physical contact with the electrode channels, allowing measurements of both conductivity (i.e., sodium concentration) and the spatial extent of fill over time. Inlet (radius ~ 1 mm) and exit ports define the bottom surface of the microfluidic substrate. The patterned skin adhesive laminated on this bottom surface creates a collection zone for excreted sweat to pool and enter the inlet port directly from the skin. An additional reinforcing adhesive layer extends laterally along the perimeter of the microfluidic substrate by 6 mm, allowing greater areal coverage and robust adhesion to the skin for extreme environments and instances of heavy sweating. This adhesive geometry creates a water-tight seal for sweat to gather in the collection zone and enter the microchannel regions without any contamination from external fluids (e.g., rain or water immersion), while providing a path for sweat from other areas to exit from under the device.

An exploded view of the electronic module (Fig. 1b) highlights major components such as a transimpedance amplifier circuit to measure sweat volume and sodium concentration, dual temperature sensors to measure skin temperature and the distal temperature slightly offset from the skin to compute the temperature inside the PPE as well as direction of radiating heat; accelerometer to estimate motion, haptic motor (Vybronics VCLP1020B002L), similar to those in mobile phones and smart watches, to provide feedback to the wearer via vibration, microcontroller with Bluetooth Low Energy transceiver (64 MHz Cortex M4 processor, ARM), and primary coin-cell battery (CR2032, 200 mAh). To achieve maximum ruggedness, the module housing covers the entire PCB and consists of a static-dissipative, glass-filled nylon to protect the internal hardware components while maintaining a spark-free exterior to support use in hazardous environments. The top surface of the housing consists of a power button and a

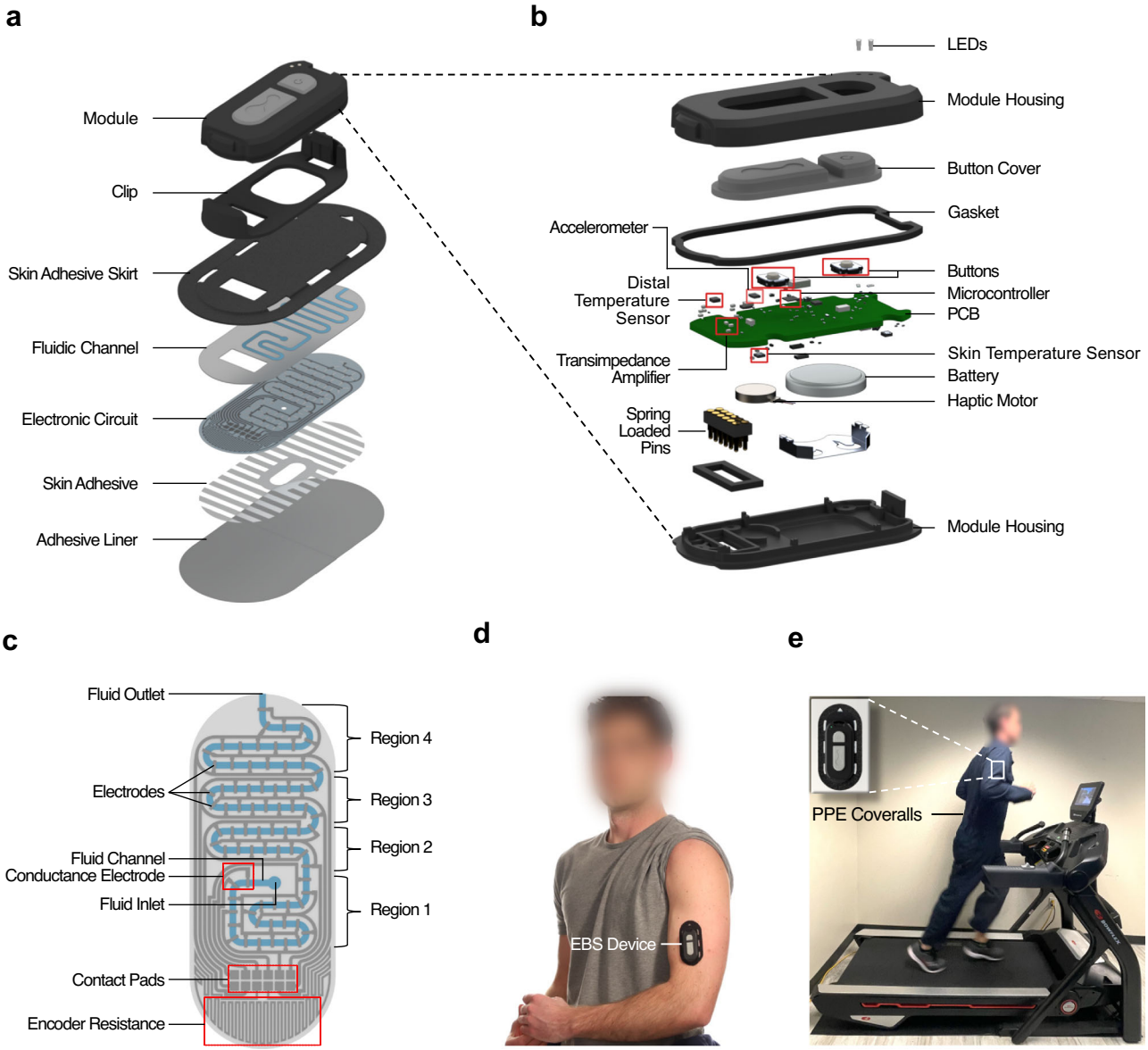

Fig. 1 | EBS device showing electrochemical sensors, biophysical sensors, associated electronics, and microfluidics substrate. a Schematic drawing of the EBS device module and exploded view of the underlying microfluidic substrate, including the microfluidic channel, electrode circuitry, and multiple capping and adhesive layers. **b** Exploded view of electronic module showing key components including battery, PCB, microcontroller, accelerometer, two temperature sensors (for thermal flux measurements), haptic motor (for vibration notifications), and pin interconnects (for electrical coupling between microfluidic substrate and module). **c** Schematic drawing of the microfluidic channel and electrode circuitry layers. **d** Photograph of fully assembled EBS device with module mechanically clipped into the microfluidic substrate and adhered to the biceps/triceps region. **e** Representative example of a subject running on a treadmill while wearing the EBS device on their biceps/triceps region underneath a PPE suit.

second larger button, easily accessible through PPE, to acknowledge and end haptic feedback. For nominal daily use, the EBS device coin cell battery supports over 1000 h of operation when used in industrial work settings where physical work may last up to ~16 h/day, without requiring daily recharging cycles. This duration of usage could also expand to 1–2 years of use for more event-driven applications in the case of athletics and fitness where active daily use is typically shorter in duration. Supplementary Figure 1 lists technical specifications of the electronic module and microfluidic substrate.

The EBS device contains 12 pins that electrically couple to the subjacent microfluidic substrate, as shown in Fig. 1b, enabling continuous measurement across multiple electrochemical sensor data streams. The electronic module couples to this substrate using a mechanical clip that locks the module in place above the microfluidic substrate. The printed circuit integrated into the microfluidic substrate is divided into 5 regions, each with an array of interdigitated electrodes as illustrated in Fig. 1c and Supplementary Figure 2a. Each of the five regions constitutes a segment of the single fluidic channel running from the inlet to the outlet. The first region consists of a short segment of the channel that has two electrode pads having a 3-mm gap between them, spanning a volume of about 1 μL. The purpose of this region is to measure the conductivity of the wearer's sweat, which to first order is proportional to sodium concentration. The 1.77 mm^2 pads are designed to cross the channel so that the electrodes conduct current once sweat reaches the second pad. The following three regions consist of longer segments of the same fluidic channel and whose purpose is to measure volume and changes in volume over time. Each of the remaining three regions consist of a single interdigitated electrode pair where the individual fingers have the same pitch as in the first region. The conductivity of sweat measured in first electrode pair is used to determine the volume in the following regions. Since the pitch is the same, the current passing through two electrode pads in these regions

is nearly identical to that of the first region (with minor variations that are handled in firmware, as described in "Methods"). The final region has a slightly larger gap of 4 mm, allowing it to span a larger volume at the cost of a slight loss in volume resolution. A long trace printed onto the fluidic substrate, marked "Encoder Resistance" in Fig. 1c, forms a fixed resistance value. This value is measured along with the other channels by the transimpedance amplifier, allowing the module to determine that it is attached to a fluidic substrate and to potentially support different substrates that can be identified by their encoder resistance.

Each region is probed by applying a 20 kHz sinusoidal voltage across the electrodes and measuring the resulting current with a transimpedance amplifier having a gain of 2 V/mA. The resulting voltage is sampled every 15 µs for 200 samples by an analog-to-digital converter (ADC) and the peak-to-peak voltage is determined from these samples. A pair of multiplexers is used to sequentially measure from each electrode pair, allowing 1.2 µs after switching for the amplifier to stabilize before taking a measurement. Because sweat conductance depends strongly on sodium chloride concentration which varies both within and across individuals, current is measured in response to 3 different excitation voltages to ensure that the signal is large but not saturated. The total time per measurement of all channels and excitation voltages is about 72 ms. Measurements are taken once every 20 s, which is sufficient to capture sweat production at physiological rates. The use of closely spaced electrodes enables high-resolution measurement of fill volume. In addition, dividing the circuit into five sets of electrode pairs allows for a higher gain of the trans-impedance amplifier, improving the signal-to-noise ratio. The 20 kHz excitation frequency was chosen to reduce depletion at the electrode surface and reduce overall measurement time while still being measurable by the ADC. Supplementary Figure 3 provides a block diagram of the EBS reusable module including this measurement process.

The module measures and records local sweat loss and sodium concentration as described above. Based on these measurements and the wearer's height and weight, the module computes whole-body fluid and sodium losses. These values are transmitted to the mobile app whenever it is in range, and any intake logged in the app is transmitted back to the module. In this way the module monitors net fluid and sodium loss for the wearer even when the mobile application is not in range. Whenever the wearer loses 500 mL of sweat, regardless of prior fluid intake, the module produces a brief (6-s) vibration with the haptic motor to remind the wearer to drink fluid. This duration was chosen to be noticeable without distracting the wearer. When the wearer reaches a net fluid loss of 2% of body mass (taking fluid intake into account), the module produces a longer (20-s) vibration to make the wearer aware that they may be dangerously dehydrated. Because these indicators have short durations, use of the haptic motor does not rapidly deplete the battery charge. Supplementary Figure 4 shows that the haptic vibration does not impact measurements of fill volume or sodium concentration.

Figure 1d shows an image of the EBS device on the biceps/triceps region of the arm. The device is designed to be applied on dry skin to ensure proper adhesion for long duration wear cycles. Here, the EBS device can be worn comfortably underneath PPE with limited risk of delamination due to arm movement or heavy lift activities. Figure 1e highlights one typical type of PPE (Nomex Coverall, DuPont) used in the industrial sector. The EBS device was exposed to high humidity (60–100%) and temperature fluctuations within the suit for long term wear cycles to test signal quality and degradation in the field.

Benchtop characterization of sweat loss, sodium concentration, and thermal effects

Figure 2a shows the benchtop testing apparatus used to perfuse saline of known sodium concentrations into the EBS device microchannels, at controlled flow rates, and with precise temperature control inside an incubator. The EBS device was positioned overlying a perfusion stage and connected to polystyrene tubing and syringe pump (located outside of the incubator) to simulate sweat excretion and flow through the EBS device. The syringe pump was programmed to perfuse systematically at different flow rates into the EBS device. Figure 2b shows the range of fluid volumes and sodium concentrations measured from one such trial using a 33.4 mM sodium chloride solution perfused at 1 µL/min (comparable to a moderate normalized sweat rate of 0.87 mg cm^{-2} min^{-1}). The raw electrical impedance data is shown in Supplementary Figure 2b and highlights fluid filling all subregions within the microfluidic channel. Discrete steps correspond to the fluid contacting each pair of electrodes, allowing the known fluid volume to be determined. An initial fill of 12.8 µL is needed to measure a signal from the conductance electrodes. From there, each electrode represents an additional fill of 1.086 µL (2.172 µL at region boundaries since two electrodes must contact fluid to complete the circuit). In region 4 the electrode spacing is increased by 1.33x to increase overall measurement volume. These measurements are summarized in Fig. 2c, indicating a strong correlation between measured and known fluid volumes and across a broad range of physiologically relevant sodium concentrations. Furthermore, these bench tests were conducted across $n = 48$ EBS devices at two temperatures (20 and 35 °C) and 8 sodium chloride concentrations (5–106 mM) to fully characterize the robustness and accuracy of the EBS sensors. Figure 2d shows that the measured voltage at a given sodium chloride concentration is temperature dependent. Based on these measurements we derived a correction factor to determine the equivalent voltage at 40 °C:

$$V_{40C} = V_{meas} \cdot 1.02^{(40-T_{meas})} \quad (1)$$

where V_{meas} and V_{40C} are the measured voltage and equivalent voltage at 40 °C, respectively, and T_{meas} is the measured temperature in °C. The temperature correction factor yielded high correlations ($R^2 = 0.95$) between measured and known sodium concentrations independent of temperature (Fig. 2e). This temperature correction factor was incorporated into EBS device firmware and applied to all measurements. Although this impedance-based method can overestimate sodium concentrations in real sweat due to the presence of other ions, because sodium chloride is the predominant salt in sweat[43] this effect is significant at only the lowest sodium concentrations. At these concentrations electrolyte losses can be replenished through food intake alone, greatly reducing the need for detailed electrolyte monitoring. Sodium measurements have been tested down to concentrations of 5 mM on bench; on-body testing values have been ≥10 mM, consistent with previous studies[44].

On-body field studies of EBS device

The time course of net fluid and sodium losses for a wearer over the course of one day (~9 h) is shown in Fig. 3a. This view combines sweat fluid and sodium loss as measured by the EBS device with beverage consumption manually entered by the wearer in the mobile application. At the start of the day, the wearer consumed an electrolyte-containing drink (as self-reported using a mobile app), resulting in a net gain in fluid and sodium. As they proceeded to sweat throughout the day, that gain turned into a deficit even though the worker consumed multiple beverages. The wearer received 8 haptic notifications over the course of the day, each vibrating the EBS device to indicate that the worker had lost 500 mL of sweat. At around 13:15 the wearer received a continuous haptic notification, indicating a net deficit of >2% of body weight. In this representative example, the wearer consumed enough fluid to return to net zero loss. In contrast, the sodium deficit continued to increase throughout the day, highlighting the importance of tracking loss and intake of both fluid and sodium. Fluid and sodium loss had similar dynamics, indicating that sweat sodium concentration over time was relatively constant for this wearer.

In addition to the electrochemical sensors and associated electronics for sweat-sensing, the EBS device contains additional sensors to provide contextual information. Supplementary Figure 5 shows a representative example of wearer EBS device data consisting of sweat and sodium losses in tandem with physiological data streams from one wearer. Raw accelerometer data, aggregated in 1-min windows and scaled logarithmically

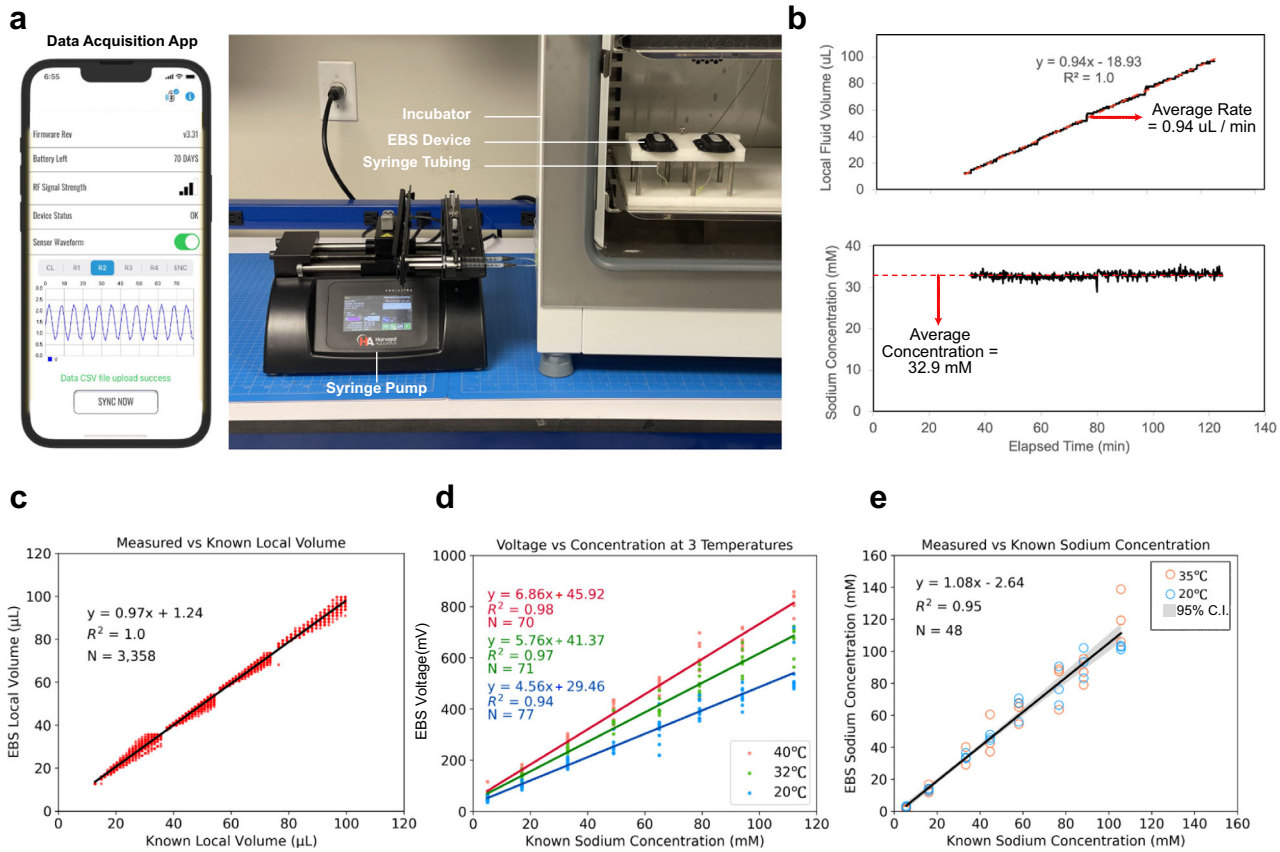

Fig. 2 | Benchtop calibration of electrochemical sodium sensor, volume and flow sensor, and temperature sensors. a Photograph of benchtop stage used to perfuse fluid through the EBS device at controlled salt concentrations, temperatures, and flow speeds. The EBS device was housed in an incubator with controlled temperature during these tests with polystyrene tubing connecting to an external syringe pump. **b** Fluid volume (top) and sodium concentration (bottom) time series data resulting from benchtop perfusion and EBS device measurements. The EBS device measured fluid fill rate (nominally 1.0 µL/min) and concentration (nominally 33.4 mM NaCl solution) during perfusion. **c** Measured fluid volume capture vs known fluid volume perfused across a range of physiological volumes indicative of sweat excretion ($n = 3358$ measurements from $n = 48$ tests; $R^2 = 1.0$). **d** Correlation of measured voltage readings vs known sodium concentrations (mM) at 3 different temperatures: 40 °C in red ($n = 70$; $R^2 = 0.98$), 32 °C in green ($n = 71$; $R^2 = 0.97$), 20 °C in blue ($n = 77$; $R^2 = 0.94$). **e** EBS device measured sodium concentrations with temperature correction applied vs known sodium concentration collected at two temperatures in the incubator. Results indicate that the EBS device effectively compensated for the temperature effects ($n = 48$; $R^2 = 0.95$). Gray shaded region indicates the 95% confidence interval (C.I.).

after subtracting the contribution of gravity, provides a measured activity score. To minimize computational processing, the logarithmic scaling is performed by simply identifying the position of the highest non-zero bit in the value. Although more precision is possible at the expense of added complexity, internal testing revealed that the precision of the current method was sufficient to distinguish between sedentary, light, moderate, and intense physical activity. To evaluate this measure, some wearers performed their exercise inside of a room calorimeter that measures metabolic rate. Figure 3b compares the EBS-measured activity score to the metabolic rate measured by a room calorimeter. The trends are similar, highlighting the ability of the EBS device's activity score to track the exertion level of the wearer.

Figure 3c compares skin temperature measured by EBS to skin temperature recordings measured by a conventional temperature sensor (iButton DS1923-F5 Hygrochron, Maxim) positioned adjacent to the EBS device. A small temperature difference arises because the EBS device's skin-side temperature sensor is separated from skin by the encapsulation and microfluidic substrate. Nonetheless, the overall trends and dynamics are similar for both measurements. Simulation results show that the skin-side temperature measured by the EBS device stays within 1 °C of true skin temperature across a broad range of ambient temperatures and heat transfer coefficients (Supplementary Figure 6). Air flow across the surface of the sensor can affect the rate at which temperatures equilibrate and the thermal gradient within the sensor, but these effects are small (Supplementary Figure 7). Note that when used without PPE for passive activity in cooler environments (e.g., office work), the measured skin temperature is lower than actual skin temperature because of the separation of the temperature sensor from skin, as represented in Supplementary Figure 8. However, under conditions that lead to sweat generation (high temperatures, physical activity) this difference quickly drops to within 1 °C.

A differentiating capability of the EBS device is the ability to estimate the thermal flux response enabled by its vertically oriented skin and distal temperature sensors. To test the stability and accuracy of this estimate, the difference between skin and distal temperature measurements was compared to thermal flux measured by a commercially available skin temperature and thermal flux monitoring device (Calera, greenTeg), as shown in Fig. 3d. The morphology of the temperature differential of the EBS device temperature sensors is strongly matched to thermal flux measured by the control Calera device, with

$$\text{Heat Flux}\left(\frac{\text{W}}{\text{m}^2}\right) = 700(t_{\text{skin},^\circ\text{C}} - t_{\text{distal},^\circ\text{C}}) + 20 \quad (2)$$

across a range of wearers, demonstrating the ability of the EBS device to estimate small temperature gradients (<0.1 °C) in real time, which correlate with thermal flux.

To characterize the performance and robustness of the EBS device requires field testing compared to established instruments. Direct

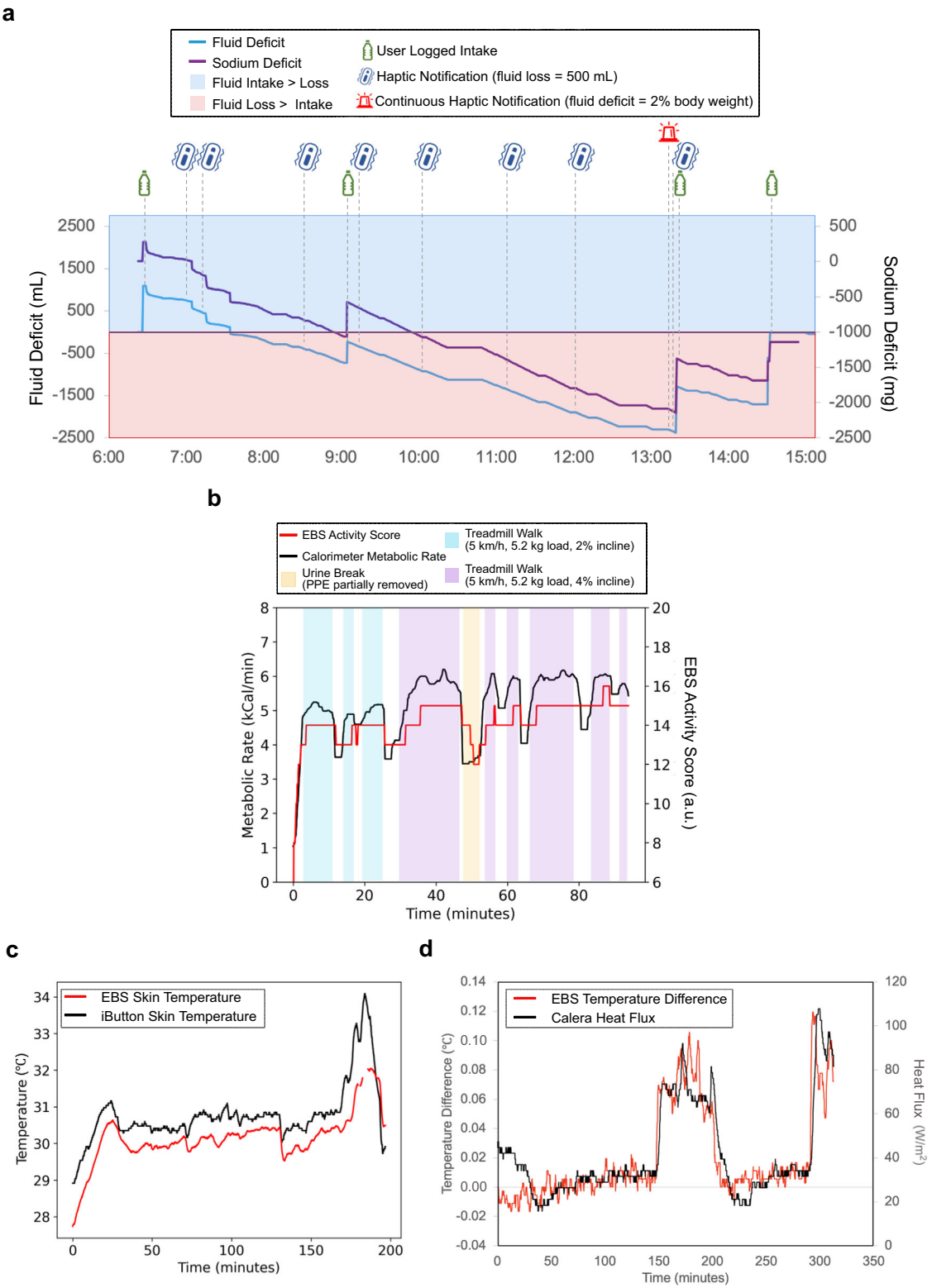

Fig. 3 | On-body time series data of sweat and sodium loss, activity level, and skin temperature. a Time series of fluid deficit (blue line) and sodium deficit (purple line) over a 9-h period. Interactions between wearer and EBS device such as logging intake (green water bottle symbol), EBS device triggering a haptic notification for sweat loss (blue vibrating module icon), and EBS device triggering a haptic notification for significant net fluid deficit (red alarm icon) are automatically logged. Shading indicates regions of net fluid surplus (blue) and deficit (red). Upward step changes are present whenever the user manually logged intake. **b** Time-aligned measured activity score as measured by EBS device (red) and metabolic rate (kCal/min) as measured by room calorimeter (black) during typical workplace activity levels (inclined walking while wearing a weighted vest). Shading indicates the type of activity performed by the wearer. Unshaded regions represent times when the wearer stood in place to rest. The activity score reflects changes in exertion as determined both observationally and by metabolic rate. **c** Time-aligned skin temperature as measured by EBS device (red) and by the adjacent iButton device (black). Changes in skin temperature are reflected in both recordings. **d** The temperature difference measured by the EBS device's two temperature sensors closely track heat flux measured by a heat flux sensor. The temperature difference data was filtered with a 10-point median filter to reduce noise.

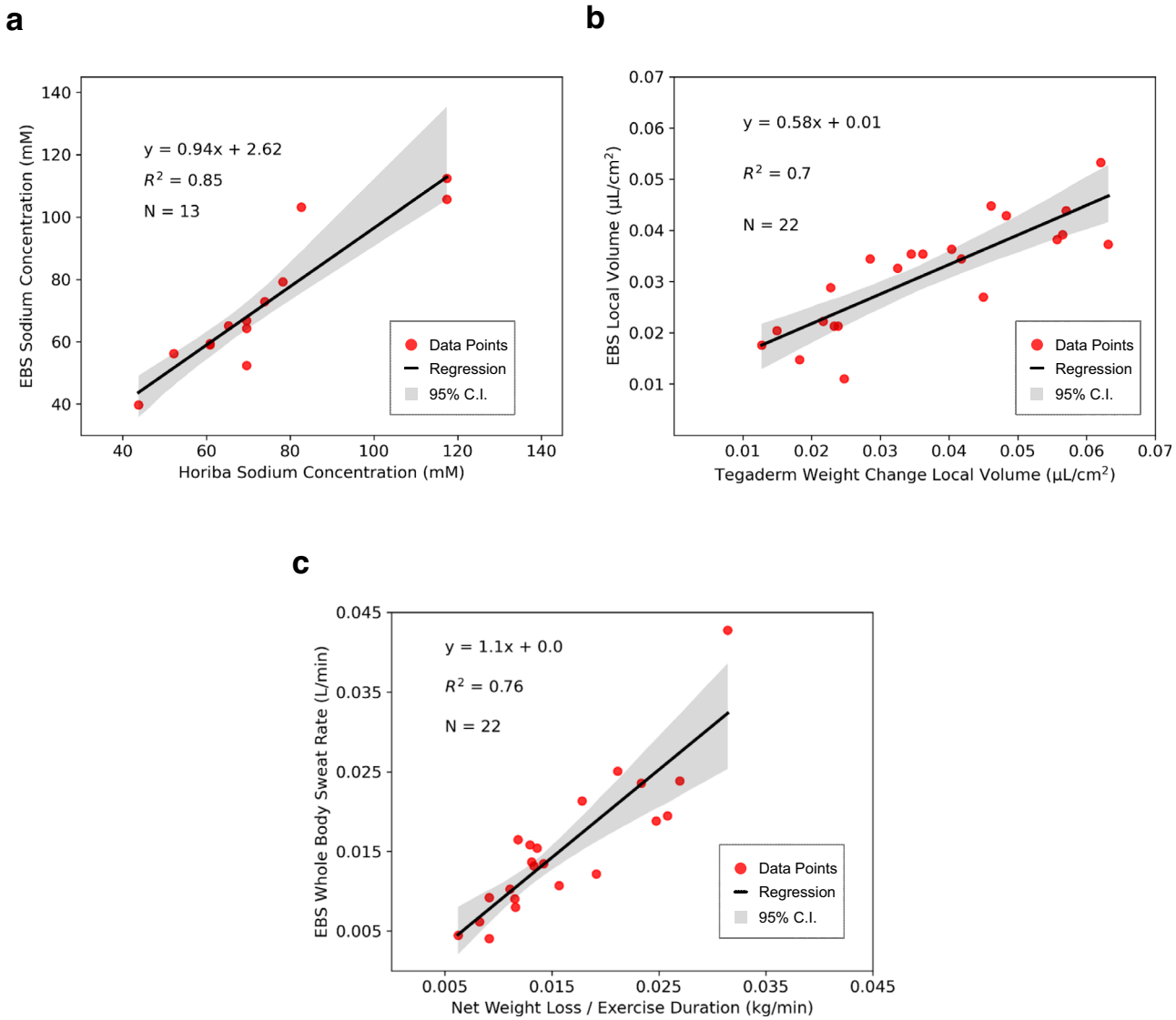

Fig. 4 | Population correlations of on-body data for sodium concentration, local sweat volume, and whole-body sweating rate. a Correlation of sodium concentration as measured by EBS with the ground truth as measured by the Horiba sodium electrode. The gray area represents the 95% confidence interval (C.I.) of the best fit (black line), which includes the line of unity. **b** Correlation of local sweat volume normalized by collection area as measured by EBS device with that measured by the net weight change of a Tegaderm pad. **c** Correlation of whole-body sweating rate (L/min) as measured by EBS device with the net weight loss rate of the subject pre- and post-exercise. The line of unity falls within the 95% CI.

measurements of sweat properties measured by EBS were compared to standard techniques, as highlighted in Fig. 4 across $n = 22$ wearers. Figure 4a shows that the EBS-measured sweat sodium concentration compares favorably to that measured with a hand-held sodium electrode ($R^2 = 0.85$; LAQUAtwin, Horiba) across $n = 13$ wearers. The range of sodium estimates covered both low-moderate to high concentrations (40–115 mM), indicating that the dynamic range is suitable for both normal and elevated sodium levels. A total of 9 subjects did not produce sufficient sweat to fill the control device used for sodium electrode measurements as noted in Fig. 4a. Similarly, the local volume measured by the EBS device is strongly correlated with absorbent-pad-measured local volume ($R^2 = 0.70$) spanning a broad range of sweat losses (0.01—0.065 µL/cm^2; Fig. 4b). The slope of this correlation is less than 1, as has been observed for other microfluidic devices compared to absorbent pads[31]. Because sweating rate varies with body location, local sweat loss measurements are mapped to whole body estimates using the ratio of body surface area to local collection area and multiplying by a location-specific scaling factor[45]. Figure 4c shows that the whole-body sweating rate measured by the EBS device is well-correlated with that measured gravimetrically ($R^2 = 0.76$) across $n = 22$ subjects, demonstrating the utility of this platform to measure whole body sweat dynamics and biocomposition metrics in active wearers over long duration cycles. Comparisons of sweat sodium concentration and whole-body sweat loss to control measurements showed comparable results when subjects did not wear PPE (Supplementary Figure 9). Moreover, these whole-body sweating rate estimates derived from the regional measurements in Fig. 4b create opportunities for presenting fluid and electrolyte replacement strategies in real-time using haptic feedback as well as in the mobile application and cloud portal, thereby enabling actionable hydration feedback to wearers.

Discussion

A key advantage of the EBS system is the real-time nature of the sweat and biophysical data streams being captured and wirelessly relayed to a smartphone. These streams are tabulated for individual wearers with automatic data transmission to a cloud portal for viewing of aggregated population data across many wearers. For a representative industrial worker use case, whereby biometric sweat and physiology data captured by the EBS device are viewable on a smartphone and relayed to the industrial worker. In parallel, individual data can be pooled across many industrial workers and

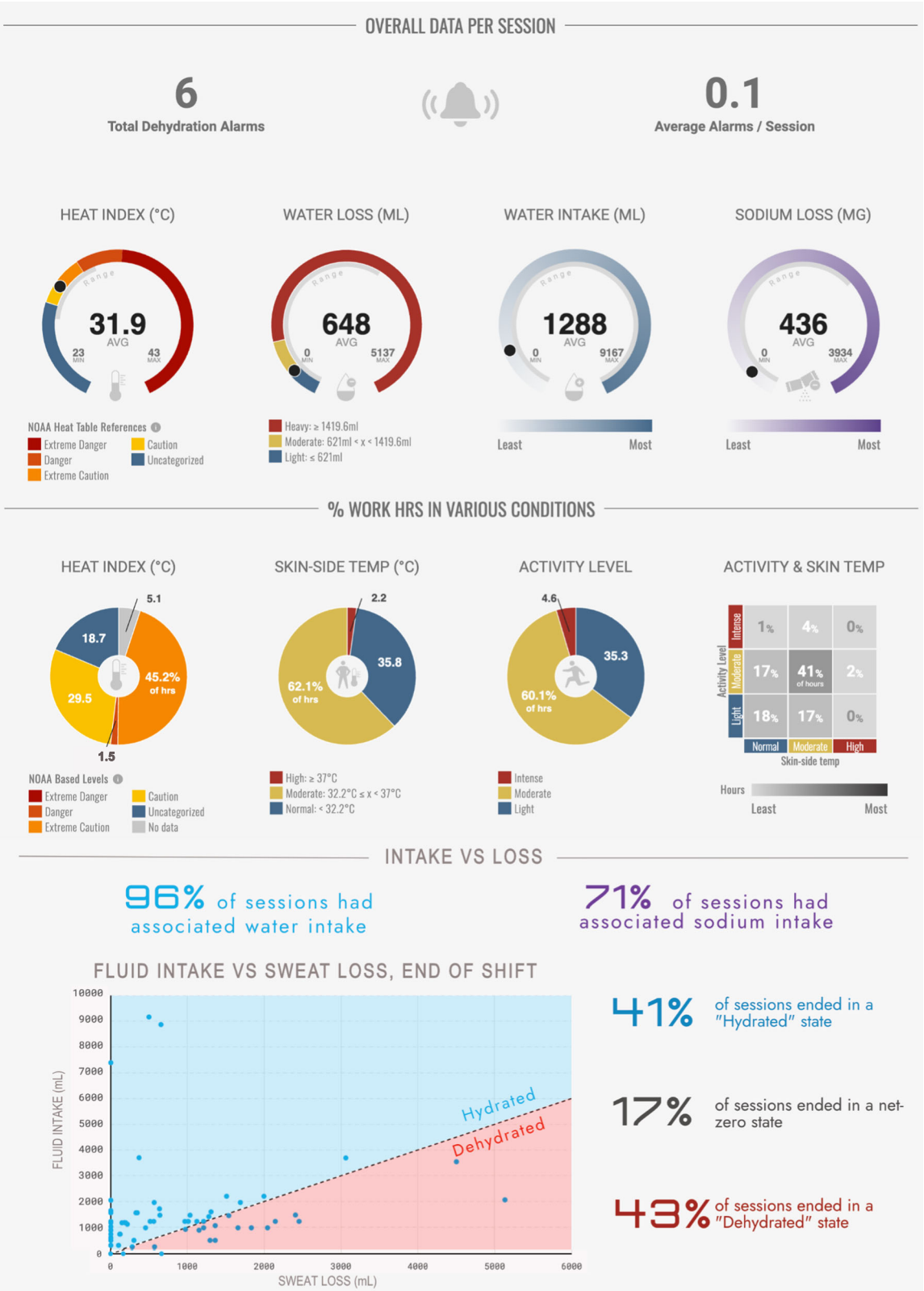

Fig. 5 | Example of supervisor view of aggregated site data in cloud portal. Data from each individual's mobile application is transmitted to a cloud portal. Population data in the cloud (e.g. heat index, average water loss, average water intake, average sodium loss, skin temperature, activity level, and fluid intake vs water loss) is aggregated and summarized for view by health and safety managers, industrial hygienists or medical personnel who review it to gain insights, anticipate risks, and identify longitudinal patterns. Managers and caregivers are empowered to communicate insights or updates to hydration safety protocols back to industrial workers.

transmitted wirelessly to a cloud portal for rapid assessment by industrial health and safety personnel, who then communicate insights and personalized safety instructions back to the industrial workers. Figure 5 shows a representative view of the cloud portal, highlighting summary statistics across a population of workers. An assortment of worker population hydration and physiology data, including the running total of haptic notifications, average number of haptic notifications per work session, average sweat loss, average sodium loss, and biophysical data are displayed, in combination with environmental data and behavioral trends. To view dynamic shifts in sweat loss over long time periods (e.g., weeks to months) for sub-groups within a population, the cloud portal provides further insight into the effects of weather patterns and work functions on hydration and physiology metrics. Finally, to track haptic notifications and rehydration actions from the EBS device and mobile application, the cloud portal compares sweat loss to the fluid intake reported for each industrial worker during a work session, showing whether workers experienced net hydration or dehydration over the course of the workday.

To promote consistent hydration practices, the EBS hardware, mobile application, and cloud incorporate key interactive features to drive awareness. The mobile application displays a fluid deficit time waveform (fluid intake minus sweat loss), indicating when the wearer's sweat loss is greater than what is replenished (Fig. 3a). In these instances, the trace dips into the negative region. This real time fluid deficit tracking capability provides feedback to the wearer to quantitatively replenish their sweat loss and input their intake in the mobile application by entering the volume of fluid replenished. These large hydration, physiology, and environmental datasets, enabled by the EBS device, mobile application, and cloud portal, inform health and safety personnel to respond in real-time with necessary changes in fluid intake, rest schedules, and other safety measures to mitigate risk of dehydration and heat stress. In summary, this end-to-end system architecture establishes a simple and dynamic portal for taking action by both industrial workers (at the individual level) and health and safety personnel (at the population level).

In summary, the EBS device enables real-time and continuous analysis of multiple sweat and biophysical metrics in combination with autonomous haptic cues and personalized feedback to preventatively combat dehydration and heat stress. Benchtop and field studies utilizing the EBS device, smartphone mobile application, and cloud compared to conventional laboratory tools demonstrate the accuracy and unique capabilities of this multimodal device to wirelessly relay electrochemical and biophysical data to a wearer and cloud portal. The robust intrinsic properties and mechanics of the EBS device to withstand significant fluctuations in ambient temperature (under PPE), intense body movements, and exposure to long duration wear cycles make this biosensor ideal for use in highly active wearers in challenging environments. The collection of features and haptic feedback demonstrated in the EBS device fundamentally changes the approach to managing hydration and physiological insights in physically demanding occupations which are impacted by extreme heat conditions.

Methods

Fabrication of EBS electronic module

The EBS module was assembled with miniaturized circuitry components and optimized PCB board layout, as illustrated in Fig. 1b. The PCB substrate and electrical tracing utilized 4 layers of laminate (370HR, Isola) and FR4 material with 34.8 μm copper in the center layers and 17 μm copper on the outer layers. Trace widths, PCB substrate core and metal layer thicknesses were determined according to computational modeling (AppCad Coplanar Waveguide Software, Agilent) to meet microstrip line impedance. The PCB is populated with commercial off the shelf components (COTS) and assembled using an automated pick and place process. The COTS components include a 64 MHz Cortex M4 ARM microcontroller with 2.4 GHz Bluetooth transceiver in a 3 mm×3 mm footprint, 3-axis 16 G accelerometer (Freescale), dual 0.1 °C ultra-low power temperature sensors (Maxim Integrated) laid out on a dedicated isolated region of the PCB, and a primary coin cell battery (CR2032, Murata). Upon completion of pick and place assembly, the PCB was then coated with acrylic (Humiseal 1A33) to protect the electronic subcomponents against water-ingress, humidity, and to meet minimum electrical creepage and clearance spacing requirements. To further protect the internal electronic components, the housing formed from injection-molded static-dissipative, glass-filled nylon, and gasket around the perimeter were oriented to create a strong water-proof barrier, as shown in Fig. 1b.

Fabrication of EBS microfluidic substrate

Standard die-cutting, laser cutting, and electrode printing techniques enabled fabrication of the microfluidic substrate. This substrate consists of a stack of thin-film elastic polymers forming the microfluidic channels, an adhesive layer interfacing with the clip fixture on the top surface, and a patterned skin adhesive layer on the bottom surface as shown in Fig. 1a. Pressure-sensitive adhesive served as the interfacing layer, bonding the sublayers of polymeric materials together. Inlet windows and windows in the adhesive layer created openings to define the sweat collection region interfacing with the skin. Patterned flexible electrodes (Ag/AgCl; 21 μm thick), extending from the inlet to the electrode regions and outlet port within the microchannel, defined the sweat flow path with known cross-sectional area and extent. For electrochemical analysis, this multi-electrode layout enabled regional sweat volume, local sweating rate estimates, and conductivity measurements in real-time.

Finite element analysis of heat transfer in EBS device

Heat transfer analysis determined the effects of thermal conduction and natural convection on the responses of the temperature sensors in the EBS device under different ambient temperatures. 3D finite element analysis (FEA) implemented in the software COMSOL 6.1 modeled the spatial temperature response of the EBS device on the skin under variable environmental conditions. A parametric sweep captured the effect of changes in the heat transfer coefficient h and ambient temperature T_{amb} when the core body temperature T_{core} was held constant at 37 °C. The skin tissue, external sensor encapsulation, and internal sensor components were modeled by 3D tetrahedron elements. The number of heat transfer elements in the model was ~1.5×10^6, and mesh convergence study was performed to ensure accuracy of the results. The COMSOL heat transfer interface was used to numerically solve the temperature according to the governing equation:

$$\rho C_p \mathbf{u} \cdot \nabla T + \nabla \cdot (-k \nabla T) = Q \tag{3}$$

where T is the temperature, ρ is the mass density, C_p is the specific heat capacity, $\mathbf{u}$ is a translational motion vector, k is the thermal conductivity of the material layers, and Q is a heat source term that is taken as zero based on the assumption that the heat generated by internal electronic components in the device is negligible as compared to the heat transfer from the core body temperature and the environmental conditions. The boundary conditions include a constant temperature (T_{core}) at the bottom surface, $z = 0$, of the skin tissue layer,

$$T|_{z=0} = T_{core} \tag{4}$$

and convective heat flux q_0 with the ambient air (T_{amb}) at the free skin surfaces, which are exposed to the environment according to the following equation:

$$q_0 = h\left(T_{amb} - T|_{z=t_{skin}}\right) \tag{5}$$

The following parameters were used in the FEA model: room temperature T_{amb} = 20° to 40°C; convection coefficient h = (5 to 30) W $m^{-2}K^{-1}$ The material properties used in the model are: thermal conductivity, heat capacity, and mass density of 0.3 W m^{-1} K^{-1}, 1460 J kg^{-1} K^{-1}, and 960 kg m^{-3} for the skin tissue; 0.21 W m^{-1} K^{-1}, 1190 J kg^{-1} K^{-1}, and 1470 kg m^{-3} for the acrylic plastic components; 0.225 W m^{-1} K^{-1}, 2100 J kg^{-1} K^{-1}, and 1350 kg m^{-3} for the temperature sensors; 0.31 W m^{-1} K^{-1}, 1700 J kg^{-1} K^{-1}, and 1160

kg m^{-3} for the glass-filled nylon parts; 0.05 W $m^{-1}K^{-1}$, 1334 J $kg^{-1}K^{-1}$, 1550 kg m^{-3} for the cotton weave; 0.04 W $m^{-1}K^{-1}$, 810 J $kg^{-1}K^{-1}$, 2500 kg m^{-3} for the PBC board; and 0.225 W $m^{-1}K^{-1}$, 2100 J $kg^{-1}K^{-1}$, and 1340 kg m^{-3} for the thermoplastic polyurethane components.

For modeling the effect of airflow, the empirical equation

$$h_c = 9 - 0.862v_a + 8.62{v_a}^{1/2} \quad (6)$$

was used to establish the relationship between h_c and v_a. This aligns with trends and curves reported by Xu et al.[46]. A time-dependent heat transfer simulation was performed for the lower bound (0.1 m/s) and upper bound (2.5 m/s) values of v_a to generate Supplementary Figure 7b. Notably, the thermal sensors are not fully exposed to convective heat transfer, as would be the case with the device's external layer. Instead, they experience both conductive heat transfer, due to the thermal gradient between the body and the device, and convective heat transfer with the surrounding environment.

Dynamic variations in airflow velocity over time were modeled using a random velocity pattern that alternates within the natural and forced convection ranges (Supplementary Figure 7c). These variations are well-captured by the simulated thermal response in the top and bottom sensors. Supplementary Figure 7d presents the transient thermal response of the sensors when the device is on the skin, with an initial sensor temperature of T0 = 30 °C. Initially, sensor temperature was influenced by convection with the environment, leading to a decrease until reaching an inflection point around 15 min. Afterward, conductive heat transfer from the core body temperature predominantly affected the sensors, resulting in an increase in temperature. The varying airflow caused dynamic changes in the slope of this increase with time.

Benchtop flow testing

Benchtop testing (Fig. 2a) used a syringe pump (PHD Ultra with Multi-Rack Adapter, Harvard Apparatus) to perfuse saline of a known sodium concentration and temperature at a known rate into the EBS device while it recorded real-time local fluid volume and sodium concentration. First, the inlet hole on the microfluidic substrate was aligned with the inlet hole on the fixture where the syringe pump tubing connects. Next, one of eight sodium chloride solutions (5.6, 16.1, 33.4, 44.7, 58.1, 76.8, 88.3, and 105.7 mM) was loaded into syringes and the syringe pump was set at a controlled flow rate. Then, EBS modules were clipped into the microfluidic substrate and placed in an incubator (Forced Air Incubator, VWR) for 1 h to reach its target temperature before initiating the syringe pump and starting recordings. Using a custom mobile application on a smartphone (iPhone SE, Apple), local volume fill and sodium concentration were monitored in real-time during the test and all raw data was downloaded to the smartphone and computer workstation (MacBook Pro, Apple) for further analysis once the test was completed. These bench tests were performed at three pre-selected temperatures (20, 32, and 40 °C). From the raw data, individual steps were identified and the voltage was measured to determine the precise mapping between voltage (relative to the conductance channel) and fill volume. While this mapping was roughly proportional to the number of electrode pairs connected by fluid for each region, variations of about ±10% were present due to channel curvature and current-dependent internal losses. These variations were included in the firmware code to compute fill volume. The same data were used to derive equations that correct for the effect of ambient temperature on measured fluid conductance (Fig. 2d). Based on these tests, a temperature correction factor of 2% per °C was employed. To test the temperature correction for the volume and sodium concentration measurements, 3 trials were performed using the same 8 saline solutions at 2 temperatures (20 and 35 °C). Sweat flow rate was held constant at 1 µL/min for each test. The results of these tests were used to create Fig. 2c, e.

Human subject testing

Subjects between the ages of 18 and 60 years old were eligible to participate in this study. This study was approved by the WCG Institutional Review Board (Puyallup, WA; IRB ID: 1364136) for the protection of human study participants. The approved protocol covers all aspects of human studies described below, except Room Calorimeter Testing which used a separate IRB as listed in that section. Subjects were informed of all experimental procedures and associated risks prior to providing written informed consent. Written informed consent included acknowledgment that photos or videos of subjects may be taken during the study, and that faces and other identifying features will be obscured. After providing written informed consent, each subject's nude body weight (to the nearest 0.01 kg), height (based on the subjects' estimate to the nearest 1 cm), and age were recorded. The main exclusion criteria were history of allergic response to skin adhesives; diagnosis of heat illness in the previous 6 months; respiratory illness; atopic dermatitis or psoriasis; heart disease, stroke or neurological condition; known cardiovascular risks; or pregnancy. In total, $n = 12$ males and $n = 10$ females were recruited in the field study.

Each subject was advised to abstain from alcohol or recreational drugs for 24 h prior to study start. In preparation for the study, subjects wore protective suits (Nomex, Dupont) to simulate the work environment of industrial workers. These suits are comprised of synthetic polymers that make the material inherently heat- and flame-resistant, but also minimally breathable, trapping body-generated heat and humidity within the suit.

During the experimental trials, subjects followed skin preparation procedures published previously[31] and were then instrumented with the EBS device as well as conventional sweat collection, heart rate, and temperature sensing devices. Subjects ran on a treadmill (Treadmill 10, Bowflex) in a hot and humid room (30 °C, 61% humidity) for 60–90 min. Heart rate was monitored using telemetry (Heart Rate Monitor, Polar) positioned on the chest. Subjects were asked to adjust their cadence to maintain a target heart rate of 80% HR_{max}, calculated as

$$\text{Target heart rate (bpm)} = 0.8\,(220 - \text{subject age}) \quad (7)$$

In a subset of trials, subjects wore an off-the-shelf skin temperature sensor (iButton DS1923-F5 Hygrochron, Maxim Integrated) adjacent to the EBS device. For thermal flux measurements and comparison, a subset of subjects also wore an established thermal flux and temperature sensor (Calera, greenTEG) on their left lateral ribcage. These comparative temperature measurements were time aligned and sampled every 10 s as shown in Fig. 3b.

To account for fluid intake and net loss, subjects were provided pre-weighed bottles of water to drink during exercise that were then weighed after consumption to the nearest 0.1 g using a compact digital scale (CX1201, Ohaus). This estimate of water consumed was used to calculate total fluid intake weight. Immediately before and after exercise, subjects dried their body with a towel and their nude body weight was recorded using a digital platform scale (Weighing Platform PBA655, Mettler Toledo) to the nearest 0.01 kg. The net body mass change and weight of water consumed were combined to determine net weight change during exercise.

Prior to exercise start time and following the initial nude weight measurement, each subject scrubbed their biceps/triceps region on both arms with an alcohol pad and waited for the skin region to dry. Once dry, the EBS device was applied to the biceps/triceps region of the left arm ahead of physical exercise. In parallel, a 10 cm^2 absorbent pad (Tegaderm Pad 3582, 3 M) was applied and adhered to the skin to collect sweat from the right biceps/triceps region. The absorbent pad and liner were weighed using a digital scale (Digital Analytical Balance, Hanchel) prior to skin application. Once the absorbent pad was applied and good adhesion was confirmed based on visual inspection, an elastic net dressing (Surgilast, American Medicals) was placed over the right biceps/triceps region to ensure that the absorbent pad remained adhered to the skin. The absorbent pads were removed after moderate sweat absorption was achieved during exercise, and prior to saturation of ~0.5 g, as previously reported[31]. The time of absorbent pad removal was noted to allow time-aligned comparisons to the EBS-reported sweat volume measurements. Upon removal, the absorbent pad was weighed along with its liner, and the weight difference was calculated to determine the volume of regional sweat collected. The absorbent pad was then separated from its adhesive layer using tweezers and placed in a syringe to extract the sweat from the pad for subsequent sodium analysis, as noted in previous

publications[31,41]. For 9 subjects, this extraction process did not produce the minimum volume of 100 µL required for analysis with the sodium electrode.

Local sweat rate was measured using the absorbent pads based on the weight of the sweat absorbed into the absorbent pad and its surface area (~10 cm^2), as well as the duration of time from the start of activity to removal time using established techniques published previously[31]. In parallel, local sweating rate from EBS was computed using the local volume reported at the time of absorbent pad removal, the elapsed time since the onset of exercise, and according to the collection area of the microfluidic substrate (~1.15 cm^2).

Sodium concentration was determined by collecting at least 100 µL of sweat from the absorbent pad. Sweat was then extracted and analyzed using a sodium electrode (LAQUAtwin, Horiba), as previously published[47]. The sodium electrode was calibrated before and after each reading using reference solutions. Results from the sodium electrode were compared to real-time and average measurements of sodium concentration from the EBS device.

Whole-body sweating rate was calculated using pre- and post-exercise nude weight, corrected for fluid intake as described above. Subjects did not void between pre- and post-exercise weigh-ins. Whole body sweating rate (kg/min) was computed by dividing whole-body sweat loss by the total duration of exercise. These sweating rate measurements based on pre- and post-exercise weights were then compared to the EBS device's whole-body sweating rate (L/min) predictions. These predictions are derived from local sweat rate using three factors: body surface area calculated from height and weight using the Du Bois formula[48], the collection area of the EBS fluidic (1.15425 cm^2), and an empirical scaling factor of 1.09267 relating local to whole-body sweat loss derived from test data. This approach is similar to a previously published whole-body sweating rate prediction model[45], with the only difference being the value of the empirical scaling factor. Because this scaling factor depends on body location, the mapping of local to whole-body sweat rate is most accurate when EBS is worn on the lateral arm between the bicep and tricep regions.

Room calorimeter testing

To characterize metabolic work, a subset of subjects wearing EBS devices on their biceps/triceps performed prescribed tasks while wearing a Nomex suit inside a room calorimeter enclosure that measured oxygen consumption, carbon dioxide production, and metabolic rate[49]. These caloric expenditure measurements (University of Massachusetts WCG; IRB ID: 1339451) were compared to the motion data captured with the EBS device, as described in Fig. 3b. Subjects were informed of all experimental procedures and associated risks prior to providing written informed consent.

Data availability

All data needed to evaluate the conclusions in the paper are present in the paper and/or the Supplementary Materials. Data sets generated during the current study are available from the corresponding authors on reasonable request.

Code availability

Portions of software code that are central to interpreting or replicating the current study are available from the corresponding authors on reasonable request.

Received: 7 September 2024; Accepted: 15 January 2025;
Published online: 01 February 2025

References

1. Francis, A. et al. Chronic kidney disease and the global public health agenda: an international consensus. *Nat. Rev. Nephrol*. https://doi.org/10.1038/s41581-024-00820-6 (2024).
2. Dunne, J. P., Stouffer, R. J. & John, J. G. Reductions in labour capacity from heat stress under climate warming. *Nat. Clim. Change* **3**, 563–566 (2013).
3. Ebi, K. L. et al. Hot weather and heat extremes: health risks. *Lancet* **398**, 698–708 (2021).
4. Wang, J. et al. Extreme heat exposure induced acute kidney injury through NLRP3 inflammasome activation in mice. *Environ. Health*. https://doi.org/10.1021/envhealth.4c00007 (2024).
5. Sontrop, J. M. et al. Association between water intake, chronic kidney disease, and cardiovascular disease: a cross-sectional analysis of NHANES data. *Am. J. Nephrol.* **37**, 434–442 (2013).
6. Roncal-Jimenez, C. et al. Heat stress nephropathy from exercise-induced uric acid crystalluria: a perspective on mesoamerican nephropathy. *Am. J. Kidney Dis.* **67**, 20–30 (2016).
7. Ebi, K. L. et al. Extreme weather and climate change: population health and health system implications. *Annu. Rev. Public Health* **42**, 293–315 (2021).
8. Johnson, R. J. et al. Climate change and the kidney. *Ann. Nutr. Metab.* **74**, 38–44 (2019).
9. Chapman, C. L. et al. Kidney physiology and pathophysiology during heat stress and the modification by exercise, dehydration, heat acclimation and aging. *Temperature***8**, 108–159 (2021).
10. Nerbass, F. B. et al. Occupational heat stress and kidney health: from farms to factories. *Kidney Int. Rep.* **2**, 998–1008 (2017).
11. Adelakun, A., Schwartz, E. & Blais, L. Occupational heat exposure. *Appl. Occup. Environ. Hyg.* **14**, 153–154 (1999).
12. Gubernot, D. M., Anderson, G. B. & Hunting, K. L. The epidemiology of occupational heat exposure in the United States: a review of the literature and assessment of research needs in a changing climate. *Int. J. Biometeorol.* **58**, 1779–1788 (2014).
13. Hancock, P. A., Ross, J. M. & Szalma, J. L. A meta-analysis of performance response under thermal stressors. *Hum. Factors* **49**, 851–877 (2007).
14. Fatima, S. H., Rothmore, P., Giles, L. C., Varghese, B. M. & Bi, P. Extreme heat and occupational injuries in different climate zones: a systematic review and meta-analysis of epidemiological evidence. *Environ. Int.* **148**, 106384 (2021).
15. Stone, J. et al. *Report of the Small Business Advocacy Review Panel on OSHA's Potential Standard for Heat Injury and Illness Prevention in Outdoor and Indoor Work Settings* (U.S. Department of Labor, Occupational Safety and Health Administration Website, 2023).
16. Ioannou, L. G. et al. Occupational heat stress: multi-country observations and interventions. *Int. J. Environ. Res. Public Health*. https://doi.org/10.3390/ijerph18126303 (2021).
17. O'Neal, E. K. et al. Runners greatly underestimate sweat losses before and after a 1-hr summer run. *Int. J. Sport Nutr. Exerc. Metab.* **22**, 353–362 (2012).
18. Leib, D. E., Zimmerman, C. A. & Knight, Z. A. Thirst. *Curr. Biol.* **26**, R1260–R1265 (2016).
19. IOC consensus statement on sports nutrition 2010. *J. Sports Sci.* **29**, S3–S4 (2011).
20. Baker, L. B. Sweating rate and sweat sodium concentration in athletes: a review of methodology and intra/interindividual variability. *Sports Med.* **47**, 111–128 (2017).
21. Casa, D. J., Cheuvront, S. N., Galloway, S. D. & Shirreffs, S. M. Fluid needs for training, competition, and recovery in track-and-field athletes. *Int. J. Sport Nutr. Exerc. Metab.* **29**, 175–180 (2019).
22. Anderson, G. B., Bell Michelle, L. & Peng Roger, D. Methods to calculate the heat index as an exposure metric in environmental health research. *Environ. Health Perspect.* **121**, 1111–1119 (2013).
23. Stewart, M. Continuous personal monitoring and personalized hydration recommendations with wearable sweat sensors to prevent occupational heat stress. *Appl. Hum. Factors Ergon.* https://doi.org/10.54941/ahfe1004205 (2023).
24. Ioannou, L. G. et al. Occupational heat strain in outdoor workers: A comprehensive review and meta-analysis. *Temperature***9**, 67–102 (2022).
25. sequeira-antunes, b. & ferreira, h. a. urinary biomarkers and point-of-care urinalysis devices for early diagnosis and management of disease: a review. *Biomedicines*. https://doi.org/10.3390/biomedicines11041051 (2023).

26. Sonner, Z. et al. The microfluidics of the eccrine sweat gland, including biomarker partitioning, transport, and biosensing implications. *Biomicrofluidics* **9**, 031301 (2015).
27. Koh, A. et al. A soft, wearable microfluidic device for the capture, storage, and colorimetric sensing of sweat. *Sci. Transl. Med.* **8**, 366ra165 (2016).
28. Gao, W. et al. Fully integrated wearable sensor arrays for multiplexed in situ perspiration analysis. *Nature* **529**, 509–514 (2016).
29. Heikenfeld, J. et al. Accessing analytes in biofluids for peripheral biochemical monitoring. *Nat. Biotechnol.* **37**, 407–419 (2019).
30. Ray, T. R. et al. Bio-integrated wearable systems: a comprehensive review. *Chem. Rev.* **119**, 5461–5533 (2019).
31. Baker, L. B. et al. Skin-interfaced microfluidic system with personalized sweating rate and sweat chloride analytics for sports science applications. *Sci Adv.* https://doi.org/10.1126/sciadv.abe3929 (2020).
32. Yang, D. S., Ghaffari, R. & Rogers, J. A. Sweat as a diagnostic biofluid. *Science* **379**, 760–761 (2023).
33. Davis, N., Heikenfeld, J., Milla, C. & Javey, A. The challenges and promise of sweat sensing. *Nat. Biotechnol.* **42**, 860–871 (2024).
34. Clark, K. M. & Ray, T. R. Recent advances in skin-interfaced wearable sweat sensors: opportunities for equitable personalized medicine and global health diagnostics. *ACS Sens.* **8**, 3606–3622 (2023).
35. Bandodkar, A. J. et al. Battery-free, skin-interfaced microfluidic/electronic systems for simultaneous electrochemical, colorimetric, and volumetric analysis of sweat. *Sci. Adv.* **5**, eaav3294 (2019).
36. Wang, M. et al. A wearable electrochemical biosensor for the monitoring of metabolites and nutrients. *Nat. Biomed. Eng.* **6**, 1225–1235 (2022).
37. Ye, C. et al. A wearable aptamer nanobiosensor for non-invasive female hormone monitoring. *Nat. Nanotechnol.* **19**, 330–337 (2024).
38. Parlak, O., Keene, S. T., Marais, A., Curto, V. F. & Salleo, A. Molecularly selective nanoporous membrane-based wearable organic electrochemical device for noninvasive cortisol sensing. *Sci. Adv.* **4**, eaar2904 (2018).
39. Torrente-Rodriguez, R. M. et al. Investigation of cortisol dynamics in human sweat using a graphene-based wireless mHealth system. *Matter* **2**, 921–937 (2020).
40. Ghaffari, R. et al. Soft wearable systems for colorimetric and electrochemical analysis of biofluids. *Adv. Funct. Mater.* **30**, 1907269 (2020).
41. Baker, L. B. et al. Skin-interfaced microfluidic system with machine learning-enabled image processing of sweat biomarkers in remote settings. *Adv. Mater. Technol.* **7**, 2200249 (2022).
42. Choi, J. et al. Skin-interfaced microfluidic systems that combine hard and soft materials for demanding applications in sweat capture and analysis. *Adv. Healthc. Mater.* **10**, 2000722 (2021).
43. Baker, L. B. Physiology of sweat gland function: the roles of sweating and sweat composition in human health. *Temperature***6**, 211–259 (2019).
44. Baker, L. B. & Wolfe, A. S. Physiological mechanisms determining eccrine sweat composition. *Eur. J. Appl Physiol.* **120**, 719–752 (2020).
45. Baker, L. B. et al. Body map of regional vs. whole body sweating rate and sweat electrolyte concentrations in men and women during moderate exercise-heat stress. *J. Appl Physiol.***124**, 1304–1318 (2018).
46. Xu, J. Evaluation of the convective heat transfer coefficient of human body and its effect on the human thermoregulation predictions. *Build. Environ*. https://doi.org/10.1016/j.csite.2021.100888 (2021).
47. Baker, L. B. et al. Validity and reliability of a field technique for sweat Na+ and K+ analysis during exercise in a hot-humid environment. *Physiol. Rep.* **2**, e12007 (2014).
48. Du Bois, D. & Du Bois, E. F. A formula to estimate the approximate surface area if height and weight be known. 1916. *Nutrition* **5**, 303–311 (1989).
49. Allerton, T. D. et al. Reliability of measurements of energy expenditure and substrate oxidation using whole-room indirect calorimetry. *Obesity***29**, 1508–1515 (2021).

Acknowledgements

We thank J. Ryan, X. Huang, M. Seib, M. Stewart, M. Wasik, S. Chan, K. Underhill, L. Reid, P. Sarmicanic, and W. Chopra for their support in defining key sensing features for industrial work use-case. This work made use of the Northwestern University's Querrey-Simpson Institute for Bioelectronics and University of Massachusetts Amherst's Center for Human Health and Performance. The portions of this study conducted at the University of Massachusetts Amherst were supported by the Massachusetts Innovation Voucher Program. No other funding was granted for this study.

Author contributions

S.P.L., A.J.A, W.L., R.G., J.A.W., D.J.C., B.K.A., J.C.S., and J.A.R. conceived the idea, designed the research and wrote the manuscript. J.C.S., A.J.A., B.J.S., D.E.W., and J.B.M. performed and were involved in the manufacturing of the sensors. S.P.L., A.P.S., and W.L. designed the hardware and wireless electronics. K.Y., S.P.L., A.J.A., T.S.D., D.E.W., and D.E.M. performed software design and software validation. R.A., J.C.S., and A.J.A. performed thermal testing and mechanical modeling. J.L.G., B.J.S., G.R.F., S.B., M.J.B., M.A.B., D.S.Y., J.C.W., M.T.M., D.E.W., and C.S. assisted in device fabrication and field testing.

Competing interests

A.J.A., S.P.L., R.G., J.B.M., and J.A.R. are co-founders of Epicore Biosystems, which develops and commercializes microfluidic devices for sweat analysis. J.C.S., B.J.S., D.E.W., J.L.G., G.R.F., K.Y., M.J.B., S.M.B., A.P.S., D.E.M., J.A.W., J.C.W., W.L., M.T.M, and T.S.D. are currently employed by Epicore Biosystems. All other authors declare that they have no competing interests.

Additional information

Supplementary information The online version contains supplementary material available at https://doi.org/10.1038/s41746-025-01466-9.

Correspondence and requests for materials should be addressed to John A. Rogers, Stephen P. Lee, Roozbeh Ghaffari or Alexander J. Aranyosi.

Reprints and permissions information is available at http://www.nature.com/reprints

Publisher's note Springer Nature remains neutral with regard to jurisdictional claims in published maps and institutional affiliations.

Open Access This article is licensed under a Creative Commons Attribution-NonCommercial-NoDerivatives 4.0 International License, which permits any non-commercial use, sharing, distribution and reproduction in any medium or format, as long as you give appropriate credit to the original author(s) and the source, provide a link to the Creative Commons licence, and indicate if you modified the licensed material. You do not have permission under this licence to share adapted material derived from this article or parts of it. The images or other third party material in this article are included in the article's Creative Commons licence, unless indicated otherwise in a credit line to the material. If material is not included in the article's Creative Commons licence and your intended use is not permitted by statutory regulation or exceeds the permitted use, you will need to obtain permission directly from the copyright holder. To view a copy of this licence, visit http://creativecommons.org/licenses/by-nc-nd/4.0/.

© The Author(s) 2025